RESONANT POLYMER DEVICES FOR ELECTRO-OPTIC MODULATION AND SENSING

Thesis

Submitted to

The School of Engineering of the

UNIVERSITY OF DAYTON

in Partial Fulfillment of the Requirements for

The Degree

Master of Science in Electro-Optics

by

Brad M. Birchfield

UNIVERSITY OF DAYTON

Dayton, Ohio

May, 2006

RESONANT POLYMER DEVICES FOR ELECTRO-OPTIC MODULATION
AND SENSING

APPROVED BY:

Joseph W. Haus, Ph.D.
Director and Professor,
Electro-Optics Program
University of Dayton
Committee Chairman

Robert L. Nelson, Ph.D.
Research Engineer,
Materials Directorate
Air Force Research Laboratory
Committee Member

Andrew Sarangan, Ph.D.
Associate Professor
Electro-Optics Program
University of Dayton
Committee Member

Donald L. Moon, Ph.D.
Associate Dean
Graduate Engineering Programs & Research
School of Engineering

Joseph E. Saliba, Ph.D., P.E.
Dean, School of Engineering

ABSTRACT

RESONANT POLYMER DEVICES FOR ELECTRO-OPTIC MODULATION AND

SENSING

Brad M. Birchfield
University of Dayton

Advisor: Dr. Joseph W. Haus

Electro-Optic modulation schemes play important roles in data transmission when

high speed and high data rates are required. In this thesis, I propose a novel type of

modulation using a reflection geometry that can also be utilized in sensing applications to

detect air born agents. It is favorable to keep certain design aspects as small as possible

such as making the operating voltage, V_π, as low as possible while maintaining

compactness for the device. Current modulation schemes are built with a push-pull type

Mach-Zehnder interferometer. The size of the device is typically several centimeters in

length and the operating voltage requirements are high.

A leaky wave polymer resonant cavity, which offers a novel modulation scheme,

was designed using a prism in the Kretschmann configuration. In the first part of this

thesis, a modeling technique for simulating a plane wave interacting with a single

boundary is discussed. This single boundary condition is trivial, however it is shown

only to see how to build upon in order to model multiple boundaries that will be

representative in the device. Altering the index of each layer, as well as the thickness and

loss parameters all yield different results. Absorption losses as well as scattering losses are difficult to quantitatively incorporate, however some bulk loss properties can be included. An experimental setup was designed and built, and samples were fabricated and tested. In the second part of this thesis, the results of the experiments with the fabricated samples are described. The data was obtained and compared with the model. Finally some conclusion were drawn as to what needs to be done in order to take this research to the next step as far as device fabrication is concerned. Some other possibilities of the device geometry that can be used in the detection of air born agents are also discussed.

ACKNOWLEDGEMENTS

TABLE OF CONTENTS

LIST OF ILLUSTRATIONS

CHAPTER I

INTRODUCTION

Modulation devices are used extensively throughout many industries in the world.

Some are more demanding than others. While the device size, speed, and power

requirements vary across the industry, new and enhanced designs are requiring that these

devices be more compact while sustaining high speed operations, low voltage (V_π)

switching, and using as little power as possible to function properly. New applications

are developing in the RF photonics field in which current approaches are starting to limit

performance. Typical Mach-Zehnder modulators that work off a push-pull type electro-

optic modulation requiring traveling wave electrodes are on the size scale of centimeters

and require a fair amount of power to operate. Interferometers are also used for

modulation schemes such as the Gires-Tournois interferometer. In this thesis, I present a

detailed analysis of a modulation scheme similar to the Gires-Tournois interferometer

only with electrodes added with the goal of producing a high speed, compact, and low

power consumption device [1]. In addition to modulation effects, the device can be

modified to detect air born agents. The geometry is ideal for the sensing of agents by

exposing an actively engineered thin polymer film on the substrate and then monitoring

the optical properties of the device in the same geometry while in the presence of the air

born agents you are trying to detect [2]. This thesis focuses primarily on the results obtained for modulation.

These studies are very important to many fields in the industry. Modulation can be used in telecommunications, audio, video, satellite applications, and countless others. The size, power, and speed aspects of this design cater extremely well for the satellite industry where these characteristics are paramount. Other applications may not require high-speed data processing. An ongoing goal, of course, is to minimize these properties along the way as much as possible. The techniques used to create this device are lower in cost when compared to the techniques used in the creation of other modulation devices. The use of polymers in the design makes the device extremely cost effective. The electrodes can be added with sputtering techniques that are covered briefly in this thesis. The construction is robust to errors and starting over again to reduce these errors does not require a large investment.

The development of this study produced many conclusions as to the practicality of the proposed design. Loss mechanisms such as absorption dictate as to whether or not this modulation device can be classified as a phase or amplitude modulator. Varying the electrode material and thicknesses was also carried out. Modeling simulations was done and compared to actual device data to validate the results.

A prism substrate was used with an index (n) of 1.785. Bulk electrode elements such as gold, indium tin oxide (ITO), and silver were sputtered onto the prisms hypotenuse. A thin film polymer layer of Polymethylmethacrylate (PMMA) and Disperse Red 1 (DR1) was spun on and then a final layer of electrode material was evaporated onto the sample. The sample was then placed in a Kretschmann configuration

that is ideal for utilization of surface plasmon effects to use as a sensing scheme [3]. The Kretschmann configuration is known to be reflection geometry and can be contrasted with the Otto configuration [4]. If the electrodes exhibit low loss, then the partially coupled and guided light (leaky waves) by the polymer thin film can then be modulated by applying a voltage across the thin film. When the output is monitored as a function of input angle, the resonances that satisfy boundary conditions will have a build up of the local electric field in the polymer film and a dip in the intensity of the reflected light.

Also, the losses associated with the thin film such as scattering, absorption, and the losses inherent to the metal electrodes such as the imaginary part of the index of refraction also attribute to the dips in intensity due to the increased electric field. These intensity modulations as a function of angle were recorded and compared to a multilayer plane wave-modeling algorithm outlined and developed in detail in chapter II. At these resonant angular positions, the system is very sensitive to changes in index. The smallest change in index will force the boundary conditions to be altered and thus the angular position of this peak will change. This will correlate to intensity shifts in the laser beams output. The following description is of an amplitude modulation scheme. A phase modulation scheme was also attempted. By aligning the sample similarly to a Teng and Man arrangement, we attempted to alter the phase, S-polarization (transverse electric, TE) or the other polarization, P-polarization (transverse magnetic, TM) [5]. The results of these experiments will be discussed in Chapter V.

Issues associated with the device are also covered in the conclusion as well as other aspects than can be explored. Aspects of the phase modulation are also considered by using the Goos-Hänchen shift [6, 7]. Design considerations, fabrication problems, and

operational issues with all the components used to make this device are all covered in detail in the following chapters. We end with experimental results and further conclusions that determine the validity of this device as far as modulation is concerned. The device design for sensing applications was not fabricated. Engineering the polymer thin film to interact with certain chemical agents will change the surface plasmon effects significantly enough to produce a detectable change in the laser's intensity or phase. Such thin films can be designed to interact strongly with chemical species through a local-field enhancement effect.

Evanescent waves that are present at the electrode and thin film boundary interact with the optical properties of the thin film. When these properties change in the thin film, the output of the light intensity or phase information will change. In addition, when the modulation of the thin film with a radio frequency (RF) signal causes the optical properties of the thin film to change, the optical beam will be modulated by the RF signal modulation of the polymer thin film. How much the thin film optical properties change is based on the nonlinear coefficient of the electro-optic chromophore in the film. Current commercially available electro-optic systems have EO activity around 100 picometers per volt (pm/v). Disperse red 1, which is the EO active chromophore we used, has a much lower EO activity (0.5 pm/V) than the leading edge chromophore systems, but it is widely available.

CHAPTER II

MULTILAYER OPTICAL FILM ALGORITHM

Before making the samples, one needs to get a feel for how the device is going to behave and what kind of performance can be expected. In the modeling we wanted to be able to monitor the phase and amplitude constituents at the same time. Methods like transfer matrix method can be utilized, however we chose to explicitly solve Maxwell's boundary conditions [8]. Now this is a static modeling, meaning that we did not model the effect of the RF signal on one of the layers being the thin film. We assumed the layer was just the non-modulated film. This will tell us where the peaks and valleys are located. The modeling of this device was done using a Matlab program. Given a single boundary with index n_1 and n_2 where an electromagnetic wave interacts with the boundary, Maxwell's equations dictate how the wave will interact. Classical results demand that the tangential components of the plane wave represented by

$$\vec{E} = E_o \cos(k\vec{z} - wt)$$ must be continuous across the boundary. Figures 2.1 and 2.2

illustrate the above for transverse electric (TE) and transverse magnetic I orientations of the plane wave with respect to the boundary. The tangential components, H_x and E_y,

must be continuous across the boundary. Since it is easier to work with the electric field components, the matrices will be in terms of the electric field. However, we need the relationship between the electric and magnetic fields to solve for all the unknowns. Both

electric and magnetic fields will be shown for completeness. This is done for a single boundary initially to show how the algorithm for the multiple boundary valued problem is constructed. Doing this for a single boundary we find two equations for two unknown amplitudes. The solution to this problem is straight forward. It is done with detail only to show how to carry it further for multiple boundaries.

For medium 1, n_1, the sum of transverse E_y and H_x components are

$$E_{oy} = E_o + E_{ro}$$

$$H_{ox} = -E_o \cos\theta_o * n_1 + E_{ro} \cos\theta_o * n_1$$

(2.1)

For medium 2, n_2, the sum of the transverse field components E_y and H_x are

$$E_{1y} = E_{to}$$

$$H_{1x} = -E_{to} \cos\theta_1 * n_2$$

(2.2)

Now by continuity of the above transverse fields at the interface we have
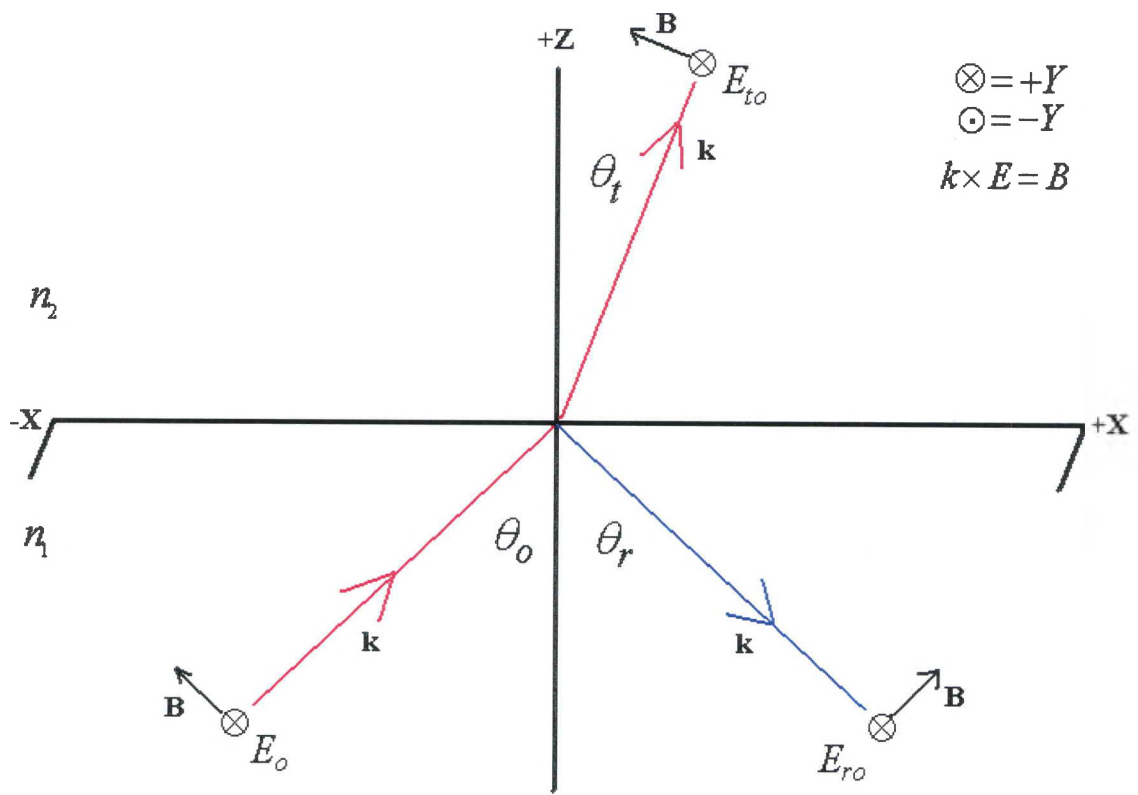
$$E_{oy} = E_{1y}$$

$$H_{ox} = H_{1x}$$

(2.3)

6

Figure 2.1: Transverse Electric single boundary.

This yields the following relationships,

$$E_o + E_{ro} = E_{to}$$

<div align="right">(2.4)</div>

$$-E_o \cos\theta_o * n_1 + E_{ro} \cos\theta_o * n_1 = -E_{to} \cos\theta_1 * n_2$$

Rearrange this in the form of

$$E_o = E_{ro} + E_{to},$$

<div align="right">(2.5)</div>

leaves the continuity equations of the form

$$E_o = -E_{ro} + E_{to}$$

<div align="right">(2.6)</div>

$$E_o \cos\theta_o * n_1 += E_{ro} \cos\theta_o * n_1 + E_{to} \cos\theta_1 * n_2$$

Now that this was obtained, using a standard math package such as Matlab, this will allow the equations to be solved. The known variables are $E_o, \theta_o, \theta_1, n_1$ and n_2.

Rewriting this in terms of a matrix simplifies the expression even more which is shown below.

$$\begin{pmatrix} E_o \\ E_o \cos\theta_o * n_1 \end{pmatrix} = \begin{pmatrix} E_{ro} \\ E_{to} \end{pmatrix} * \begin{pmatrix} -1 & n_1 \cos\theta_o \\ 1 & n_2 \cos\theta_1 \end{pmatrix}$$

<div align="right">(2.7)</div>

Figure 2.2: Transverse Magnetic single boundary.

This is of the form

$$A = B*C,$$

(2.8)

which has the solution for the electric field vector

$$A*C^{-1} = B.$$

(2.9)

Similarly, the transverse magnetic can be derived as

$$H_{oy} = E_o * n_1 + E_{ro} * n_1$$

(2.10)

$$E_{ox} = -E_o \cos\theta_o + E_{ro} \cos\theta_o$$

in medium one and

$$H_{1y} = E_{to} * n_2$$

$$E_{1x} = -E_{to} \cos\theta_1$$

in medium two.

Equating the components to ensure continuity yields

$$H_{oy} = H_{1y} \Rightarrow E_o * n_1 + E_{ro} * n_1 = E_{to} * n_2$$

(2.11)

$$E_{ox} = E_{1x} \Rightarrow -E_o \cos\theta_o + E_{ro} \cos\theta_o = -E_{to} \cos\theta_1$$

Rearranging these in the form outlined above as

$$E_o = E_{ro} + E_{to}$$

(2.12)

produces

$$E_o * n_1 = -E_{ro} * n_1 + E_{to} * n_2$$

(2.13)

$$E_o \cos\theta_o = E_{ro} \cos\theta_o + E_{to} \cos\theta_1$$

Writing this in matrix form would be

$$\begin{pmatrix} E_o * n_1 \\ E_o \cos\theta_o \end{pmatrix} = \begin{pmatrix} E_{ro} \\ E_{to} \end{pmatrix} \begin{pmatrix} -n_1 & \cos\theta_o \\ n_2 & \cos\theta_1 \end{pmatrix}. \tag{2.14}$$
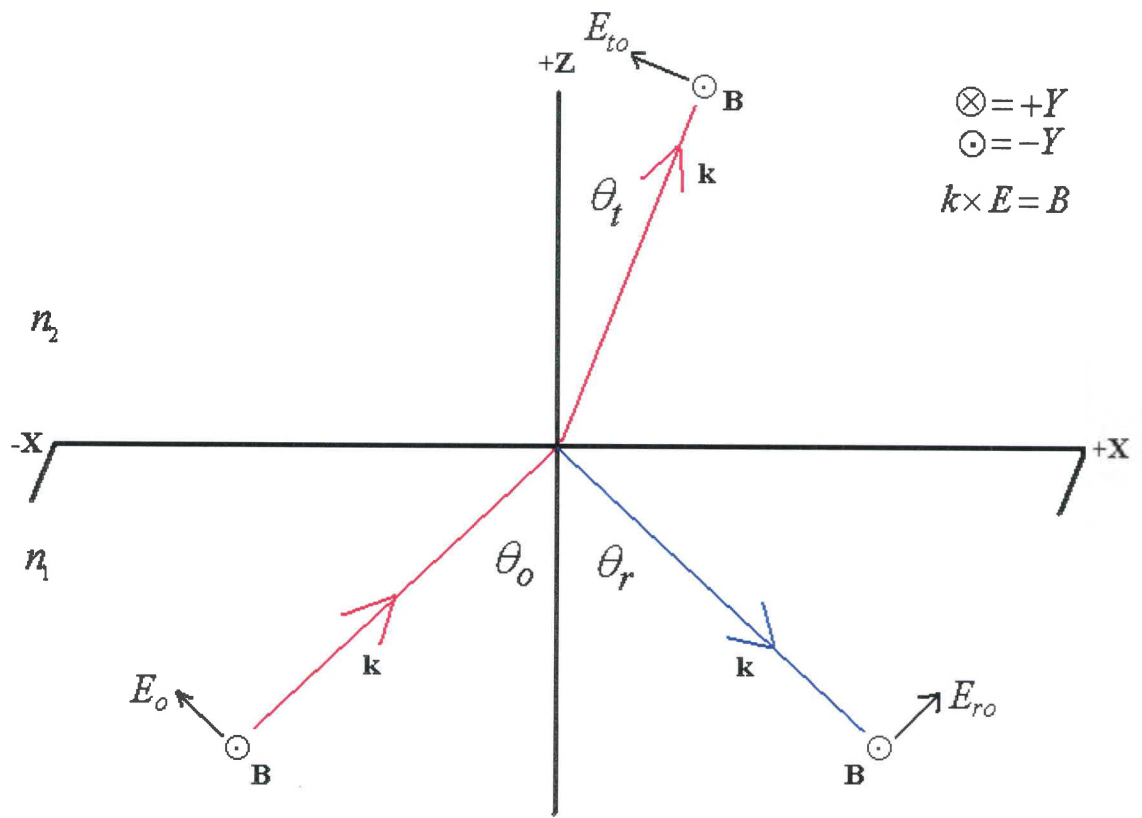
Similarly this is of the form

$$A = B * C, \tag{2.15}$$

which has the solution for the electric field vector of

$$A * C^{-1} = B. \tag{2.16}$$

Now that Maxwell's wave equations have been solved for an electromagnetic plane wave impinging on a single boundary, this method can easily be programmed into Matlab and evaluated. Since this is just a single planar boundary, one would expect the linear algebra results to parallel the Fresnel coefficients which are given for TE and TM polarizations respectively [9, 10]. This done as to verify the results of the above linear algebra.

$$r_{TE} = \frac{E_{ro}}{E_o} = \frac{n_1 * \cos\theta_o - n_2 * \cos\theta_1}{n_1 * \cos\theta_o + n_2 * \cos\theta_1}$$

$$t_{TE} = \frac{E_{to}}{E_o} = \frac{2 * n_1 * \cos\theta_o}{n_2 * \cos\theta_1 + n_1 * \cos\theta_o}$$

$$\tag{2.17}$$

$$r_{TM} = \frac{E_{ro}}{E_o} = \frac{n_2 * \cos\theta_o - n_1 * \cos\theta_1}{n_1 * \cos\theta_1 + n_2 * \cos\theta_o}$$

$$t_{TM} = \frac{E_{to}}{E_o} = \frac{2 * n_1 * \cos\theta_o}{n_2 * \cos\theta_o + n_1 * \cos\theta_1}$$

A plot of the Fresnel coefficients versus θ can be done and compared to the linear algebra technique outlined above. The reflection coefficients,

$$R = |r|^2$$
(2.18)

can be plotted for a beam emerging from within a higher index medium, n=1.5, and traversing into a lower index medium, n=1. Total internal reflection, TIR, which is where the transmission goes to zero and all the light is now reflected and can be found by,

$$\theta_c = \sin^{-1}\left(\frac{n_1}{n_2}\right) = 41.8°.$$
(2.19)

The Brewster angle which is defined as the angle at which the reflected intensity goes to zero for the TM polarization found by,

$$\theta_B = \tan^{-1}\left(\frac{n_1}{n_2}\right) = 33.7°.$$
(2.20)

The transmission can also be plotted. The Fresnel transmission is given by

$$T = |t|^2 \bullet \frac{n_2 \cos\theta_t}{n_1 \cos\theta_o}.$$
(2.21)

Again the Brewster angle for which the reflection goes to zero and the transmission goes to unity is seen as well as the critical angle for which the reflection goes to unity and the transmission goes to zero. Figures 2.3 and 2.4 show the plots of the linear algebra technique outlined above.
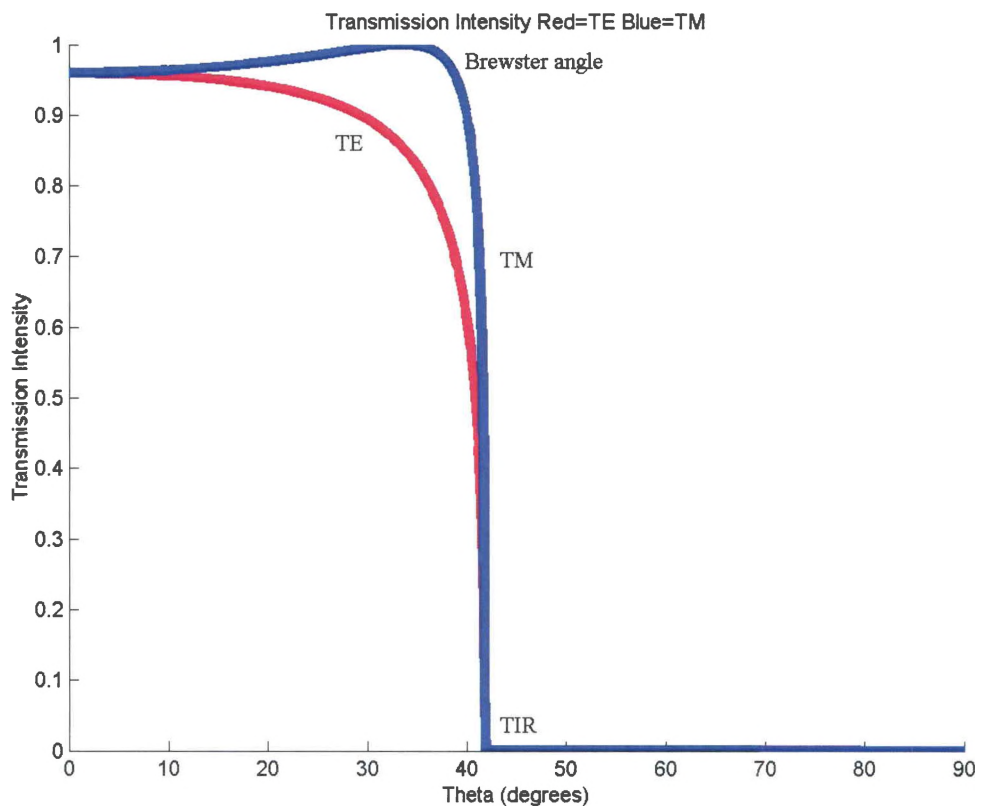
Figure 2.3: Transmission Intensity using linear algebra technique.
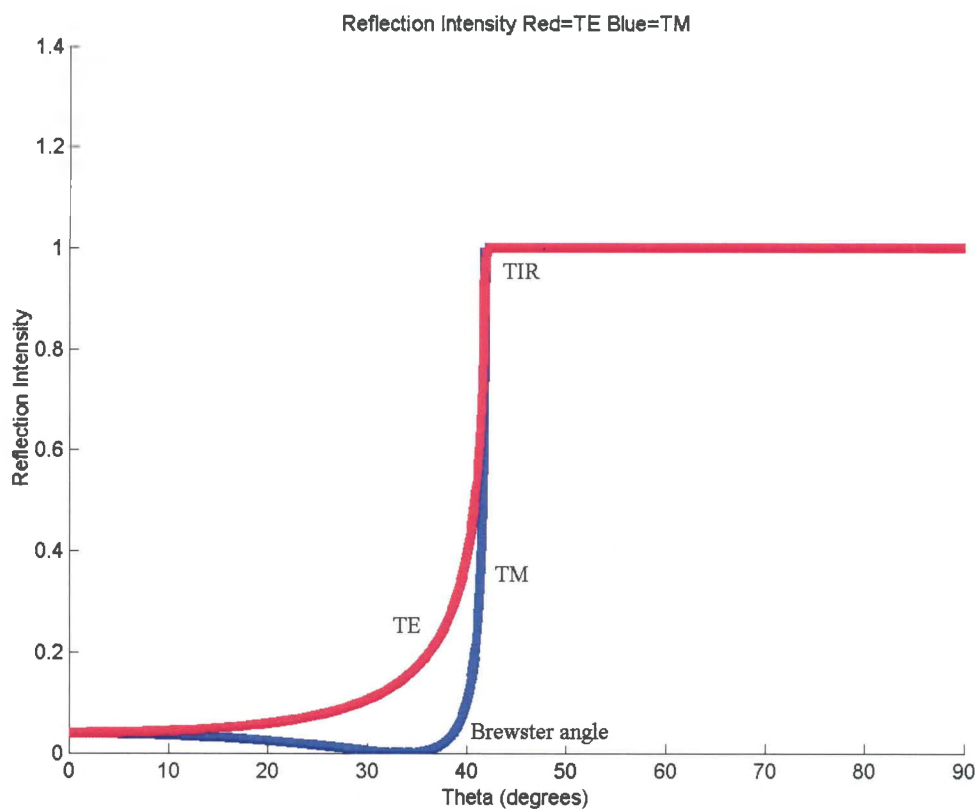
Figure 2.4: Reflection Intensity using linear algebra technique.

The two plots agree exactly with a plot of the Fresnel reflection and transmission plots. They should agree since solving the boundary equations above directly will yield the Fresnel coefficients. Since the samples are constructed such that the light is propagating from a higher index medium to a lower one, the above plots are indicative of this fact. The relative intensity of the reflected and transmitted light must add to unity to satisfy the conservation of energy

$$R = \frac{E_r{}^2 * n_o * \cos\theta_o}{E_i{}^2 * n_o * \cos\theta_r} \Rightarrow \frac{E_r{}^2}{E_i{}^2} \qquad (2.22)$$

Since $\theta_o = \theta_r$, everything cancels leaving the intensity. This is the same for TE or TM polarized light. For transmission we have,

$$T = \frac{E_t{}^2 * n_2 * \cos\theta_t}{E_i{}^2 * n_1 * \cos\theta_o} \qquad (2.23)$$

which is also valid for TE and TM polarizations. This allows the modeling to conserve energy and keep the following relationship valid,

$$R + T = 1. \qquad (2.24)$$

In order to obtain the proper matrices for a thin film, the above calculations need to be altered to account for a beam propagating across a boundary, through a thin film, and then across another boundary. Figure 2.5 below shows this geometry for TE polarization. Simply using the Fresnel coefficients at both boundaries will not give a good representation of what is actually happening. The phase, ϕ, from the Fresnel coefficients is not plotted . This can be held accountable by modifying the above approach for the

thickness of the film and then adding the phasor components. For $\theta > \theta_c$ the

reflectivity is unity reflectivity becomes $r = |r_o| e^{i\varphi}$.
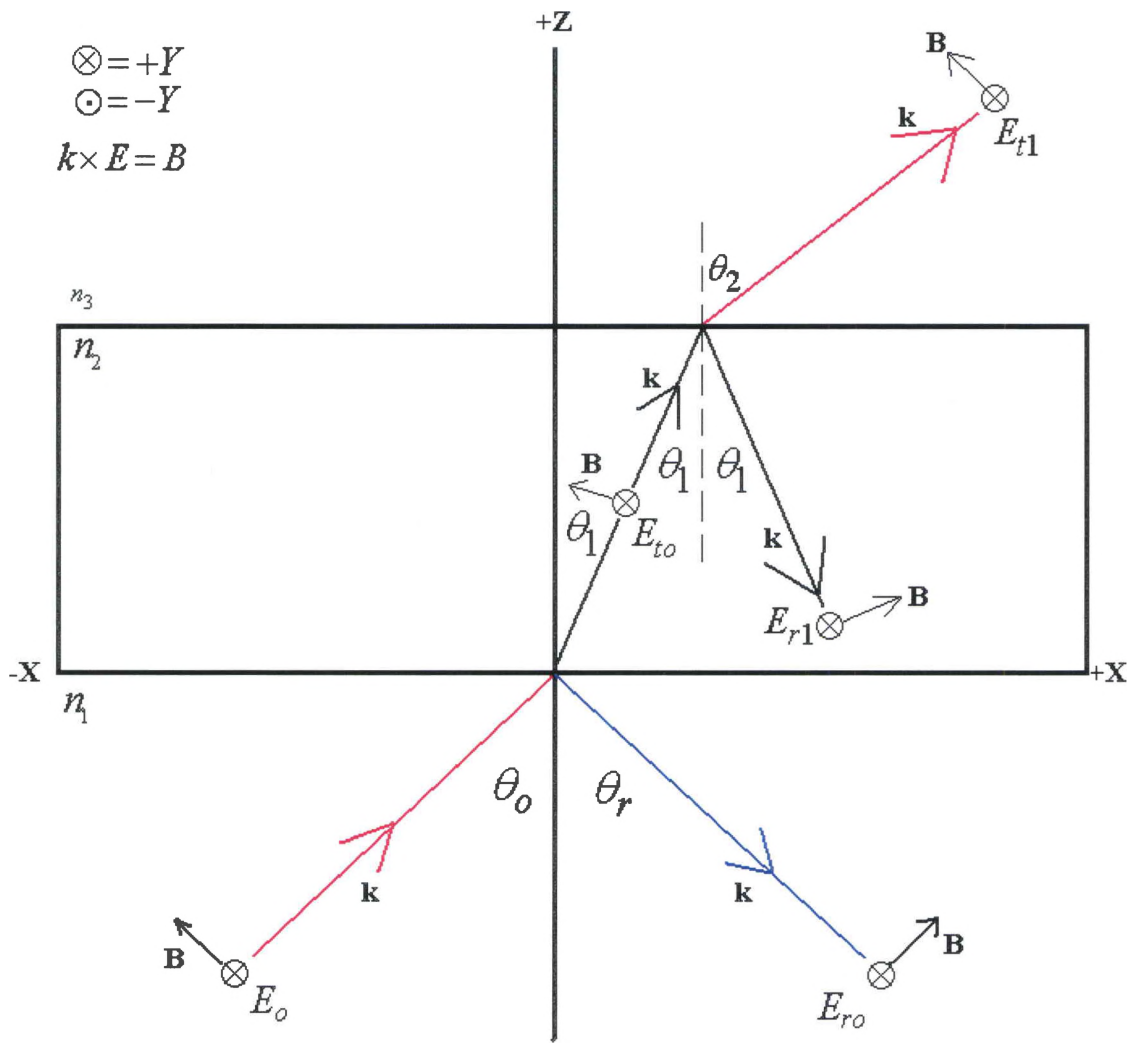
Figure 2.5: Transverse Electric through film.

Following the approach taken earlier, there are now three differing layers composing two boundaries instead of one. The sum of the field components in medium one, n_1, for TE polarization are

$$E_{oy} = E_o + E_{ro}$$

$$H_{ox} = -E_o \cos\theta_o * n_1 + E_{ro} \cos\theta_o * n_1$$

(2.25)

For medium two, n_2, we have

$$E_{1y} = E_{to} + E_{r1}$$

$$H_{1x} = -E_{to} \cos\theta_1 * n_2 + E_{r1} \cos\theta_1 * n_2$$

(2.26)

For medium three, n_3, we have

$$E_{2y} = E_{t1}$$

$$H_{2x} = -E_{t1} \cos\theta_2 * n_3$$

(2.27)

As before, setting the components equal to each other at the boundaries will ensure continuity with the addition of one extra boundary, which is done by setting

$$E_{oy} = E_{1y}, \ H_{ox} = H_{1x}$$
$$E_{1y} = E_{2y}, \ H_{1x} = H_{2x}$$

(2.28)

This will give the two boundary conditions as

$$E_o + E_{ro} = E_{to} + E_{r1}$$

$$-E_o \cos\theta_o * n_1 + E_{ro} \cos\theta_o * n_1 = -E_{to} \cos\theta_1 *_{n2} + E_{r1} \cos\theta_1 * n_2$$

$$E_{to} + E_{r1} = E_{t1}$$

$$-E_{to} \cos\theta_1 * n_2 + E_{r1} \cos\theta_1 * n_2 = -E_{t1} \cos\theta_2 * n_3$$

(2.29)

Rewriting these in the form outlined above

$$E_o = E_{ro} + E_{to} + E_{r1} + E_{t1} \qquad (2.30)$$

will allow you to see how they go into matrix form.

$$E_o = -E_{ro} + E_{to} + E_{r1} + 0E_{t1}$$

$$E_o \cos\theta_o * n_1 = E_{ro} \cos\theta_o * n_1 + E_{to} \cos\theta_1 *_{n2} - E_{r1} \cos\theta_1 * n_2 - 0E_{t1}$$

$$0E_o = 0E_{ro} + E_{to} + E_{r1} - E_{t1}$$

$$0E_o = 0E_{ro} - E_{to} \cos\theta_1 * n_2 + E_{r1} \cos\theta_1 * n_2 + E_{t1} \cos\theta_2 * n_3$$

(2.31)

Also at this point, I will add the phase information. The phase information is kept in

$$\varphi_j = e^{\pm ik_j}$$

$$k_j = n_j * \cos\theta_j * k_o . \tag{2.32}$$

$$k_o = \frac{2 * \pi}{\lambda_o}$$

The $\pm$ in the exponential represents the forwards or backwards traveling wave in the z

direction. Lambda, λ_o, is the free space wavelength of the laser. Putting all this into

matrix notation yields the following.

$$\begin{pmatrix} E_o \\ E_o\cos\theta_o \\ 0 \\ 0 \end{pmatrix} = \begin{pmatrix} E_{ro} \\ E_{to} \\ E_{r1} \\ E_{t1} \end{pmatrix} \begin{pmatrix} -1 & n_1\cos\theta_o & 0 & 0 \\ 1 & n_2\cos\theta_1 & e^{i*k_o*n_2*\cos\theta_1} & -n_2*\cos\theta_1*e^{i*k_o*n_2*\cos\theta_1} \\ 1 & -n_2\cos\theta_1 & e^{-i*k_o*n_2*\cos\theta_1} & n_2*\cos\theta_1*e^{-i*k_o*n_2*\cos\theta_1} \\ 0 & 0 & -e^{i*k_o*n_3*\cos\theta_2} & n_3*\cos\theta_2*e^{i*k_o*n_3*\cos\theta_2} \end{pmatrix} .$$

$$\tag{2.33}$$

Since this is of the same format as stated earlier, it can be solved using Matlab. Similarly

for TM polarization in medium one, n_1,

$$H_{oy} = E_o * n_1 + E_{ro} * n_1$$

$$\tag{2.34}$$

$$E_{ox} = -E_o \cos\theta_o + E_{ro} \cos\theta_o$$

For medium two, n_2,

$$H_{1y} = E_{to} * n_2 + E_{r1} * n_2$$

(2.35)

$$E_{1x} = -E_{to} \cos\theta_1 + E_{r1} \cos\theta_1$$
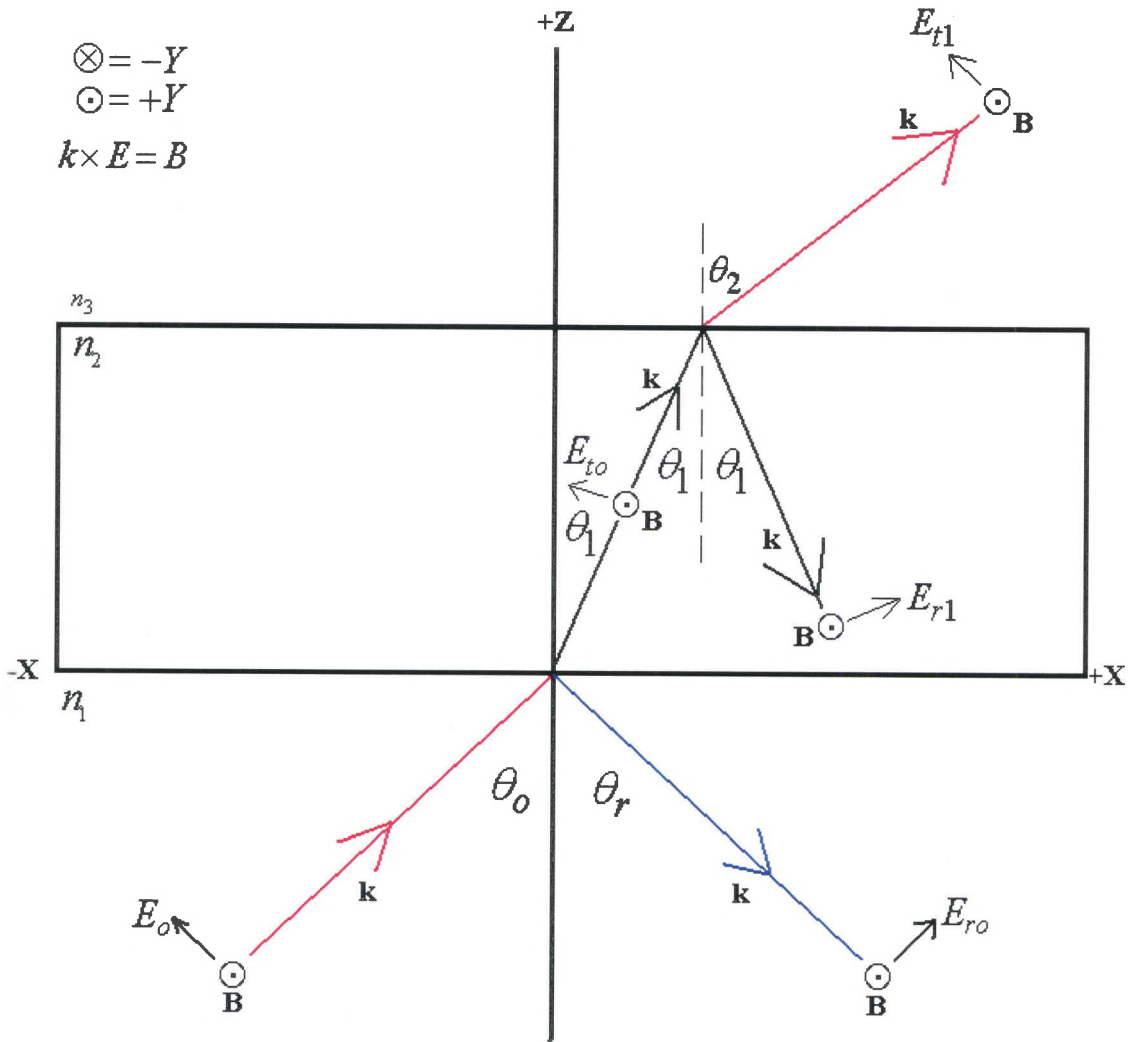
Figure 2.6: Transverse Magnetic through film.

For medium three, n_3,

$$H_{2y} = E_{t1} * n_3$$

(2.36)

$$E_{2x} = -E_{t1} \cos \theta_2$$

Equating the boundary conditions as

$$H_{oy} = H_{1y}, \ E_{ox} = E_{1x}$$

(2.37)

$$H_{1y} = H_{2y}, \ E_{1x} = E_{2x}$$

yields,

$$E_o * n_1 + E_{ro} * n_1 = E_{to} * n_2 + E_{r1} * n_2$$

$$-E_o \cos \theta_o + E_{ro} \cos \theta_o = -E_{to} \cos \theta_1 + E_{r1} \cos \theta_1$$

(2.38)

$$E_{to} * n_2 + E_{r1} * n_2 = E_{t1} * n_3$$

$$-E_{to} \cos \theta_1 + E_{r1} \cos \theta_1 = -E_{t1} \cos \theta_2$$

Maintaining the form outlined above

$$E_o = E_{ro} + E_{to} + E_{r1} + E_{t1}$$

(2.39)

yields,

$$E_o * n_1 = -E_{ro} * n_1 + E_{to} * n_2 + E_{r1} * n_2 + 0E_{t1}$$

$$E_o \cos\theta_o = E_{ro}\cos\theta_o + E_{to}\cos\theta_1 - E_{r1}\cos\theta_1 - 0E_{t1}$$

. (2.40)

$$0E_o = 0E_{ro} + E_{to} * n_2 + E_{r1} * n_2 - E_{t1} * n_3$$

$$0E_o = 0E_{ro} - E_{to}\cos\theta_1 + E_{r1}\cos\theta_1 + E_{t1}\cos\theta_2$$

Gather all this and putting it into matrix formalism in addition to adding the phase information yields the following,

$$\begin{pmatrix} E_o*n_1 \\ E_o\cos\theta_o \\ 0 \\ 0 \end{pmatrix} \begin{pmatrix} E_{ro} \\ E_{to} \\ E_{r1} \\ E_{t1} \end{pmatrix} \begin{pmatrix} -n_1 & \cos\theta_o & 0 & 0 \\ n_2 & \cos\theta_1 & n_2*e^{i*k_o*n_2*\cos\theta_1} & -\cos\theta_1*e^{i*k_o*n_2*\cos\theta_1} \\ n_2 & -\cos\theta_1 & n_2*e^{-i*k_o*n_2*\cos\theta_1} & \cos\theta_1*e^{-i*k_o*n_2*\cos\theta_1} \\ 0 & 0 & -n_3*e^{i*k_o*n_3*\cos\theta_2} & \cos\theta_2*e^{i*k_o*n_3*\cos\theta_2} \end{pmatrix}$$

(2.41)

Again, this is now in the format that has been outlined above and is easily solved using Matlab. Doing this gives us the following output shown in figure 2.7. The indices were

$$n_1 = 1.78$$
$$n_2 = 1.49 + .005i$$
$$n_3 = .3 + .4i$$

I added a little bit of loss in the PMMA layer and the gold reflecting layer. Since DR1 does exhibit an absorption band near that of a Helium neon laser, adding some loss to that layer is appropriate. Also, after poling, the gold layer is hazed and develops a noticeable

surface roughness. As the incident angle increases the critical angle is approached, which is seen in the plot as the reflectivity approaches unity. The varying intensity modulations get sharper and the maxima are closer together as TIR is approached due to the higher reflectivity at both surfaces, which gives a better quality cavity. Using a higher index prism enables us to probe more angles and to observe more resonance peaks. This is the reason so many oscillations are observed in figure 2.7.

An amplitude modulator is made by rotating the sample to a high slope region of one of the sharper resonances near the critical angle. In the example here we use the second resonance with its minimum around 54°. The higher slope is chosen at an angle slightly smaller than the angle of the reflection minimum. The sample is positioned at a point where the slope is nearly linear and we then apply a sinusoidal voltage across the active layer. For this case the intensity will be lowest when the induced Δn was negative. When the induced change in index is the largest, the intensity would approach the maximum since changing the index is equivalent to an angular shift in the intensity profile shown below. This effect is shown in figure 2.8 which plots the reflection coefficient intensity versus Δn. The angle was fixed and then the reflection was plotted as the index changed. This plot allows an analysis of the index change that is needed to obtain a certain depth of modulation. The largest slope is 28.888 and for a 50 V maximum sinusoidal voltage the index change for DR1 is found by,

$$\Delta n = \frac{V \bullet r_{33} \bullet n^3}{l \bullet 2} = 1.24x10^{-5}.$$
(2.42)

The change of the reflection coefficient can be approximated by the following function which is a linear fit to the linear region of the resonance outlined above by

23

$$\Delta I_{ntensity} = 26.888 * \Delta n + .0201.$$
(2.43)

The change in index was found using V=50 volts, r_{33}=.3pm/v, and l=2μm. Using this

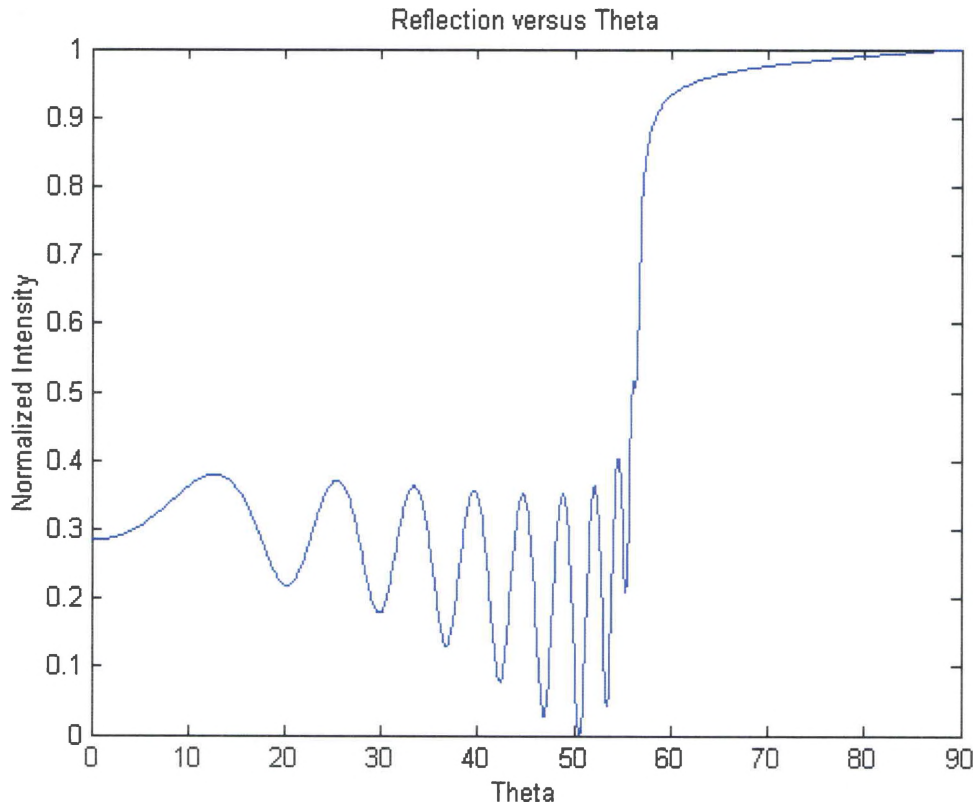value in equation 2.43 gives a depth of modulation of .02%.

Figure 2.7: Modeling output.
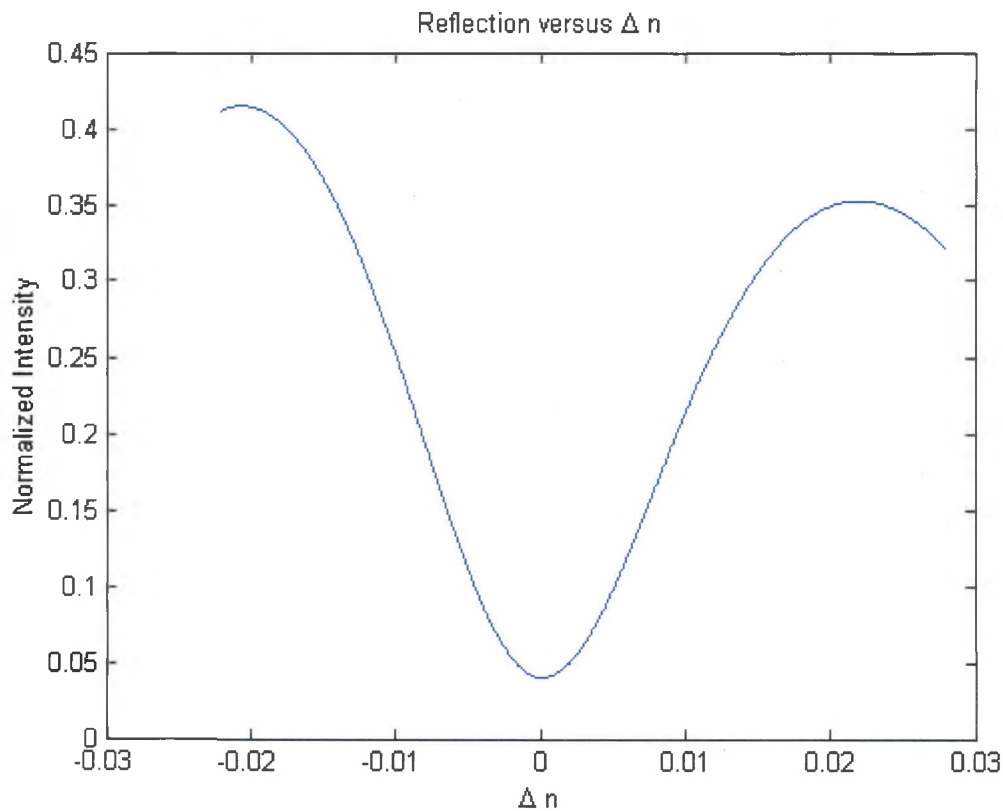
Figure 2.8: Reflection versus change in index.

This will be compared to the experimental results in the next chapter. Now, as mentioned

previously, we can model some basic bulk properties by including an imaginary

component to the index of refraction. For the electrodes, the complex index is well

known for silver and gold [11]. ITO can be very difficult to characterize in terms of

optical properties, since our ITO was deposited by in-house sputtering deposition, the

optical parameters as well as the conductivity depend on the deposition processing and

therefore it deviates from what is reported in the literature. The thin film index of

refraction can also have a loss factor included in the modeling, however scattering is not

explicitly accounted for and is observed in our samples, as we will see in our

experimental results. There are some approaches for modeling, to a degree, the amount

of scattering, for example by adding a thin layer or another set of boundaries into the

equations that have loss. By varying the thickness of this additional layer, the results will better reproduce the experimental observations. However, this method is not established with a theoretical foundation. There are a myriad of other possibilities that can be tried to obtain a good approximation of the characteristics of the actual device.

The reflected phase modulation concept was the first idea that we explored. The amount of change in the index needed to produce a pi/2 phase shift would be

$$\varphi = \frac{2\pi\Delta n \bullet \cos\theta \bullet d}{\lambda} = \frac{\pi}{2}. \tag{2.44}$$

Since the setup of the experiment involves a polarizer and an analyzer, the light would then be cycled on and off producing the modulation. The phase amount can also be solved for d, the lateral distance the center of the beam travels inside the sample, which is called the Goos-Hänchen shift. Solving for d reveals that there are many oscillations through which the phase would constructively and destructively interfere. The distance d is small compared to the distance estimated as the Goos-Hänchen shift. This simply shows that there is indeed a lot or room inside the leaky wave structure that can be utilized in the Goos-Hänchen shift for modulation purposes. This goal of an amplitude phase induced modulator and the results will be covered in chapter V.

CHAPTER III

EXPERIMENTAL DESIGN

Experimental Setup

The experimental setup is sketched in figure 3.1; it is comprised of various

components. A helium neon laser, Coherent model # 31-2066-000, with an output of 15

mW, randomly polarized is the source. The station stage is composed of two motorized

Aerotech rotation stages, model number ART310-G108, that were mounted on a manual

Newport rotational Z-axis mount, model number 487, and a single axis position stage,

shown on the left in the photograph (figure 3.2). With these additional mounts the

maximum amount of adjustment of the rotation stages could be made to accommodate

various sized samples. This setup proved to be very robust. Two Glan-Thompson Calcite

polarizer mounts could be added to the experiment; they were placed inside manual

rotation stages from Newport, model number 10GT04AR.14. One is shown in figure 3.2

between the letters B and C. A standard silicon detector connected to a Keithly Digital

Multimeter, model number 195A; the detector is shown on the left in figure 3.2. A

Stanford Research model number SR510 lock in amplifier was used in acquiring the data.

The Aerotech stages were controlled via General Purpose Interface Bus (GPIB) by a

standard desktop PC with Visual Basic (VB). The two stages sat above each other

(shown in figure 3.2) and were indexed at varying degrees down to .001 degrees. The

sample was positioned on the top rotation stage and the rotation axis was centered on the front facet of the sample. While the top stage was indexed at θ, the bottom stage which had the detector mounted to it was indexed at 2θ as shown in figure 3.3. This is all done via the PC to keep the beam centered on the detector. By rotating the detector by 2θ the beam remains aligned on the detector. At point A, the analyzer, 2nd polarizer, can be added to the setup in addition to a Soleil-Babinet compensator at point B. Attempts were made to experimentally measure the Goos-Hänchen shift by adding another rotating polarizer at point C. Further discussions on these measurements are concluded in the results section.
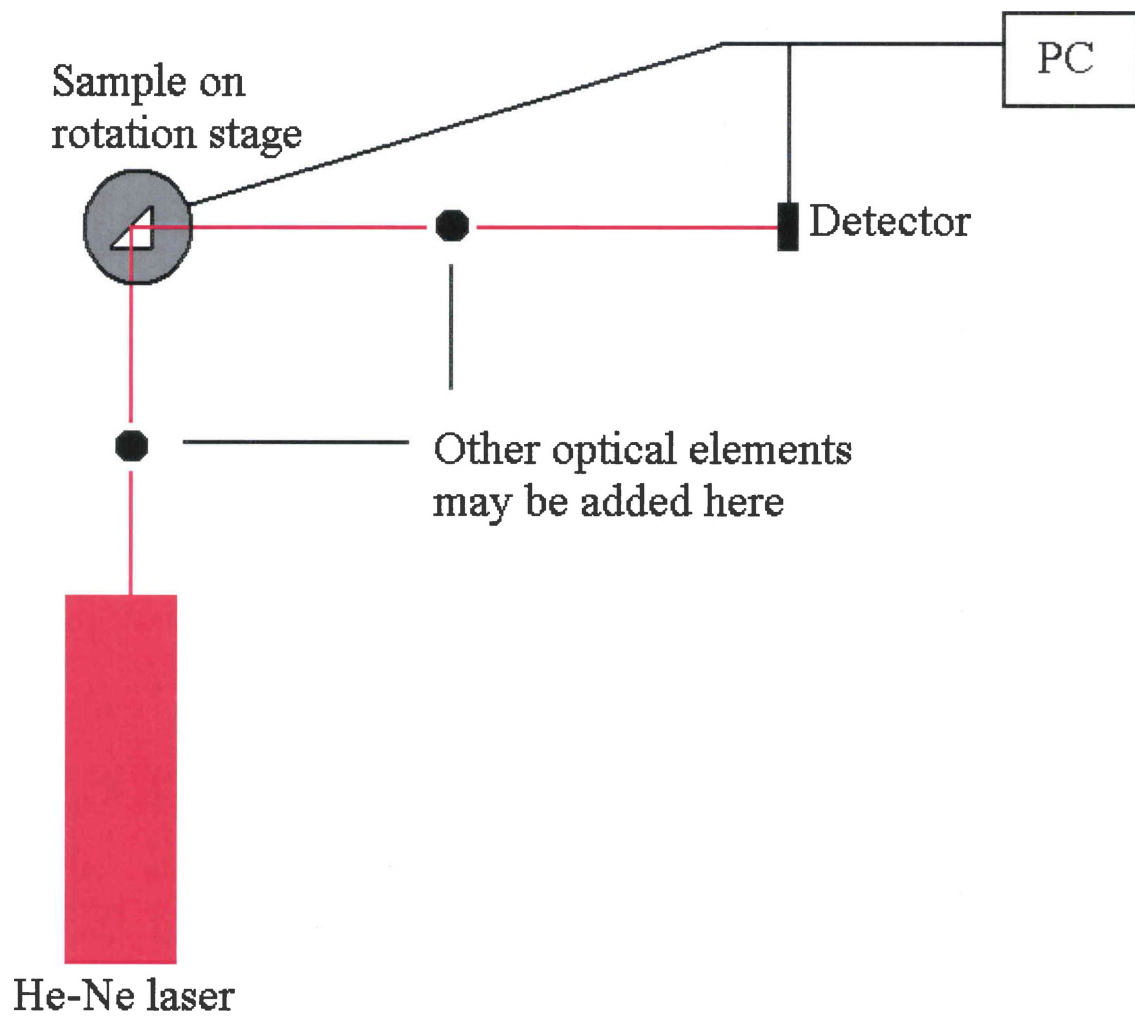
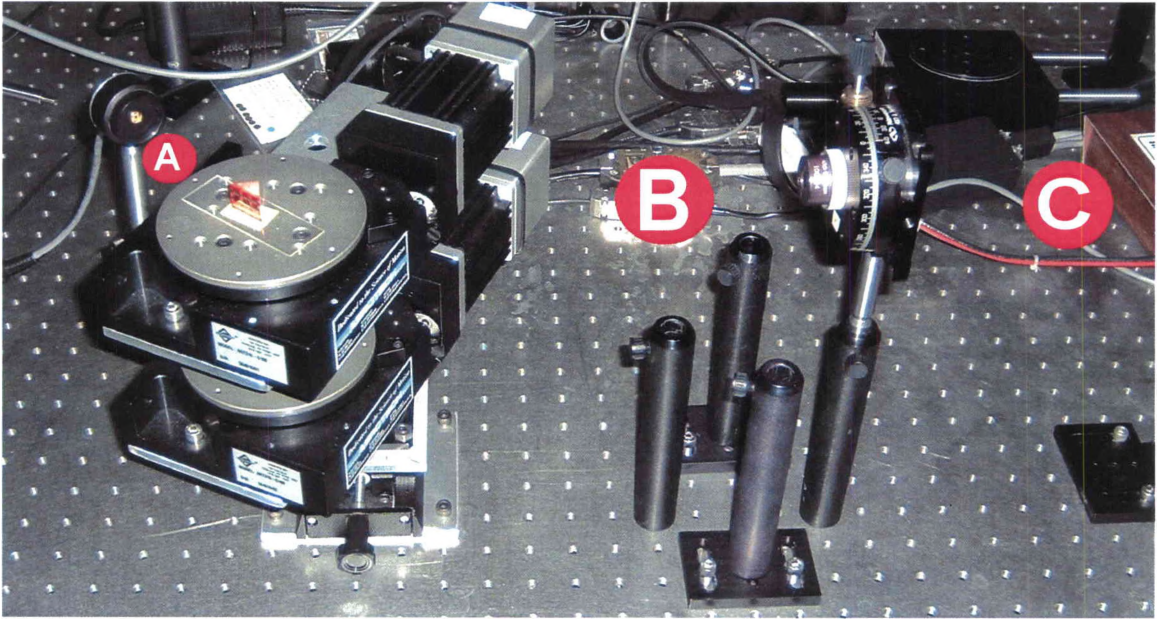Figure 3.1: Outline of experimental setup.
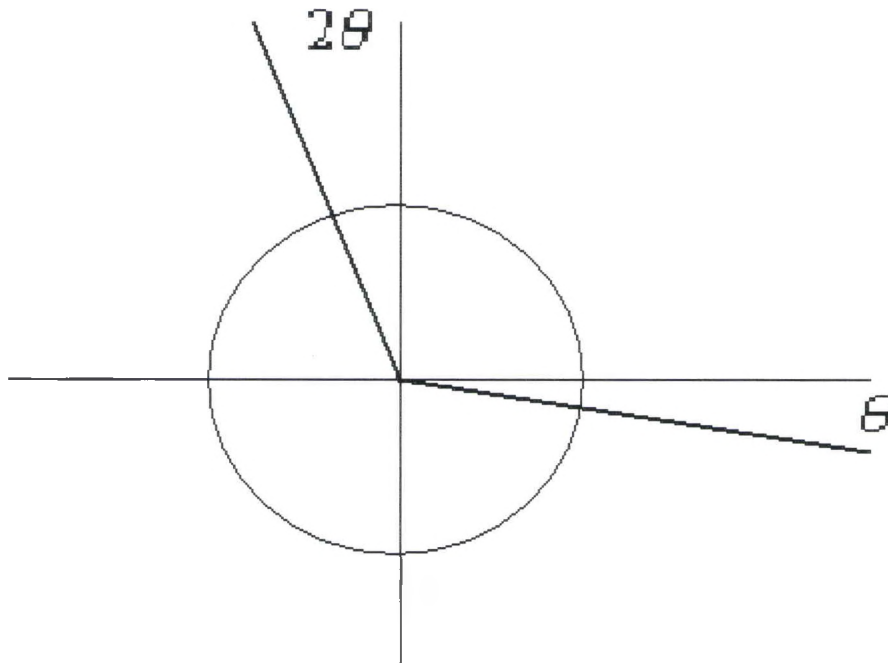
Figure 3.2: Sample measurement assembly.

Figure 3.3: Top view of the two rotation stages. The top stage rotates through an angle θ and the bottom stage rotates through the angle 2θ as shown.

At each point, the intensity and position was recorded by the PC via the Keithley multimeter. There are two turning mirrors that take the laser beam and align it with the optic axis. The first optical component is the spatial filter and recollimation assembly. This is not needed for the experiment; however it was added due to the use of the turning mirrors in order to clean up the beam. This is not shown in figure 3.2. The following element is a calcite polarizer followed by the sample. This allows the selection of transverse electric (TE) versus transverse magnetic polarization (TM). After going through the sample, the beam then reflects to the detector. In order to analyze the relative polarization phase shift, the insertion of another polarizer, the analyzer, is needed. Also a Soleil-Babinet compensator is needed after the first polarizer.

The samples where made out of SFL11 glass. These right angle prisms have an index, n, of 1.778 at the operating wavelength of the Helium Neon laser. The sellmeier equations for SF11 glass can be found at www.us.schott.com. The sellmeier equations provide a relationship between the index of the material and wavelength of the light being used. For SF11 the index is given as,

$$n = \sqrt{1 + \frac{A_1 \bullet \lambda^2}{\lambda^2 - B_1} + \frac{A_2 \bullet \lambda^2}{\lambda^2 - B_2} + \frac{A_3 \bullet \lambda^2}{\lambda^2 - B_3}} \Rightarrow 1.778622902 \quad (3.1)$$

where,

$$A_1 = 1.73848403, \ A_2 = .31116897, \ A_3 = 1.17490871$$

$$B_1 = .0136069, \ B_2 = .06159605, \ B_3 = 121.922711$$

$$\lambda = .6328 \mu m$$

31

Bulk planar electrodes of indium tin oxide were deposited via sputtering. The electrodes were 30nm thick. The electrode has to be semitransparent and only thin films of gold or silver can be used that allows light to pass into the polymer film. Next, a thin polymer film was spin coated onto the hypotenuse of the prism. The spin parameters contained a two second ramp up to 1000 revolutions per minute (RPM) and then held at that RPM for 30 seconds. After this the sample was placed in a heated oven at 60° C for 30 minutes. Next another 30nm thick layer of ITO was sputtered onto the top of the polymer film. This was the method used to create our samples. A simplified picture of the sample is illustrated in figure 3.4. A photograph of a sample is shown in figure 3.5.
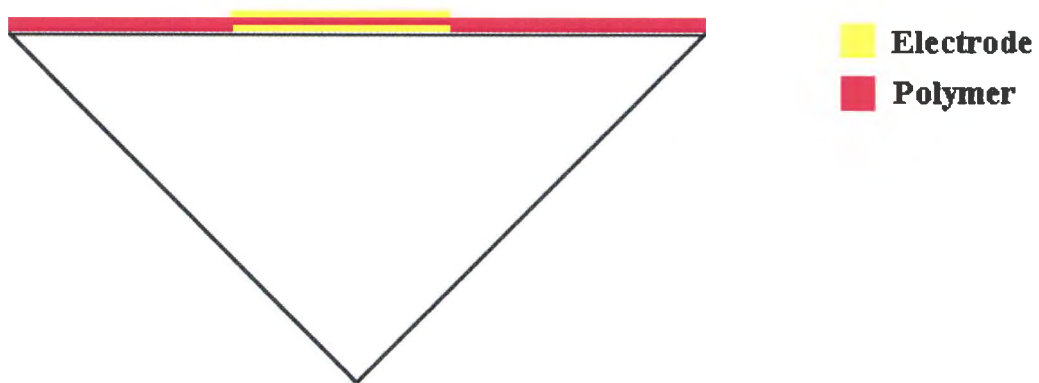
Electrode
Polymer

Figure 3.4: Simplified sample.
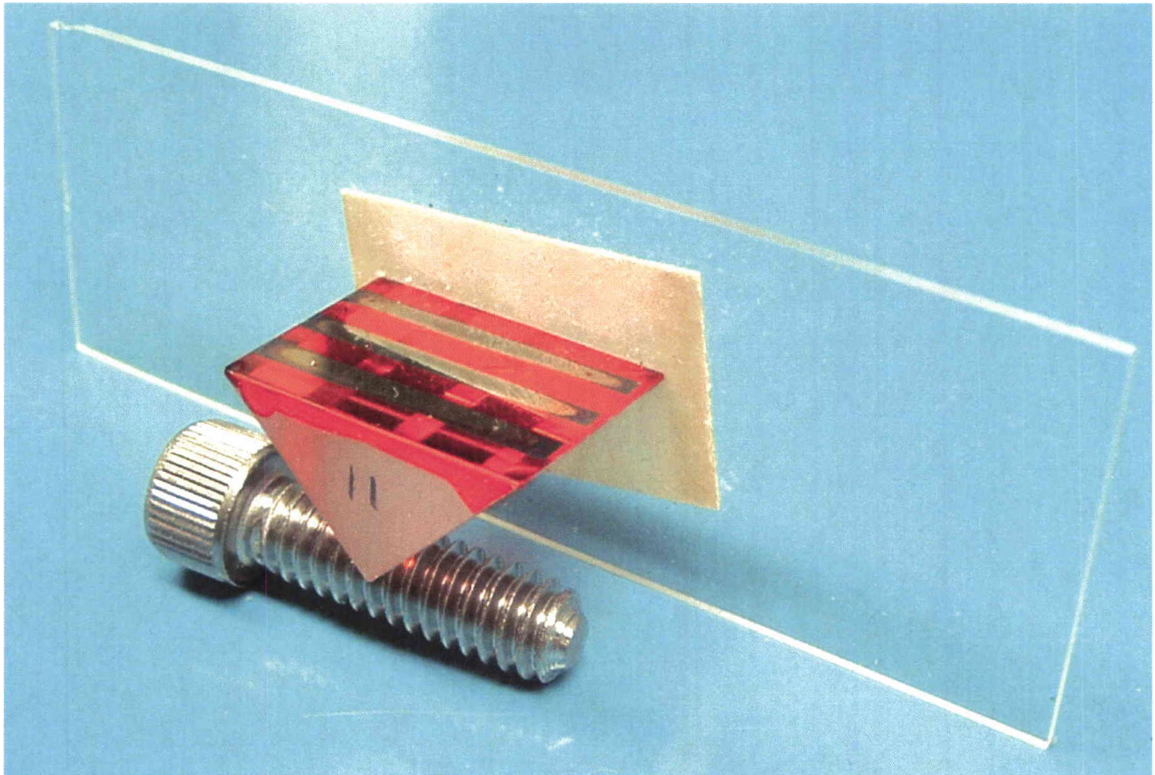
Figure 3.5: Actual sample without wire contacts. The screw demonstrates the

sample dimensions.

The top electrodes are easily seen on the sample. Underneath the top electrode is a red polymer film that has DR1 dissolved in it. The bottom electrode lies underneath the polymer layer. Three more electrode stripes oriented perpendicular to the top three electrode stripes can be observed. The contacts for the voltage source, gold wires, are applied with a conductive paste and are not shown in figure 3.5.

The polymer film composed of Disperse Red 1 (DR1), Polymethylmethacrylate (PMMA), and a solvent. There are a number of solvents used in the film deposition process, for example cyclopentanone, chloroform, acetone, etc. These solvents are chosen for their specific properties, such as, boiling point, resistivity, polarity, and

solubility. They all have varying impacts on the final quality of the thin film being made. The solutions we formulated are comprised of 30% by weight (%wt.) of PMMA to solvent. The solvent cyclopentanone consistently yielded the best results. 8 % by weight of DR1 was added to the solution. The solution was then tumbled for one hour in a temperature controlled oven at 60° C. The solution was then filtered through a series of .2µm filters to remove any undissolved PMMA or DR1. Placing the samples in a vacuum oven should be avoided. The decrease in pressure causes the solvents with low boiling points to rapidly evaporate or boil. This boiling action will cause micro voids in the sample which will lead to scattering of the light thru the thin film. This formulation with the given spin parameters yielded a 2µm film. The film has a clear red appearance with no haziness or particles visible under a low power (100X) optical microscope.

CHAPTER IV

APPROACHES TO THIN FILM DEVELOPMENT

Thin films have been produced for a number of years now. Many different approaches have been used to create a better thin film. Qualities such as surface roughness, pits, film transparency, thickness, voids, gradients, etc., etc. have always found a way to be cumbersome when creating a thin film. Some of these processes are reviewed in this chapter starting with thin polymer film deposition then moving to metal or dielectric film deposition [12, 13].

Dip Coating

Dip coating is the process of creating a solution and then simply dipping the substrate or sample into the solution. Typically this process yields a film with a modulated thickness for more viscous solutions. Less viscous solutions have a more uniform thickness and also yield a thinner film. However, this method is very cheap to use and maintain. The film thickness can be relatively uniform.

Aerosol Deposition

A relatively newer method involves using a solution that is thin enough to be sprayed on. These films tend to have a higher surface roughness. Thickness is determined by the dwell time on the target area as the solution is sprayed on. While relatively new to the

processing world, more development work needs to be performed in order to obtain consistent results.

Spin Coating

This process is used widely across the electronics industry. The start up cost is relatively low and film quality can be controlled in a number of ways. Adjusting the ramp up times and the time the sample is held at one particular speed will alter the thickness and uniformity of the film. Typically the sample is placed on the spinner and a vacuum is usually activated in order to hold the sample onto the spinning stage. Solvents, solutions, etc., etc. are then applied to the sample or substrate. After this has been done, the stage starts spinning and the excess solution is then spun off of the sample. Different ramp times, set stepped RPM's, and differing viscosities of the solution need to be experimented with in order to obtain a nice smooth film. This is the process that was used in this thesis to create the samples.

Sputtering

Radio frequency (RF) sputtering is one of the various techniques used in the creation of the samples. RF sputtering is used most often when dielectrics need to be deposited. One of the undesirable characteristics of this method is the thermal stress applied to the system. When sputtering dielectrics onto a low glass transition (T_g) polymer, it can melt the polymer. In addition to this, when depositing different types of dielectrics, the thermal stress can cause the layers to crack and flake off due to the different temperature of coefficient of expansion of the two or more materials. The glass transition temperature is the defined as the temperature at which the polymer mechanical properties changes from a brittle solid, such as glass, to a more elastic, such as rubber, material.

36

Direct current (DC) sputtering is used when metals are deposited on the surface of the sample or substrate. The metal deposition rate can be rather large and due to this, the thermal shock to the sample is minimized. This is the process we used in creating the electrodes on our samples. Typically gold, silver, or Indium tin oxide (ITO) was the electrode materials. The optical properties of the metals are well known. ITO being more transparent in the visible regime than the two metals offers a good transparent electrode. However, one problem with the ITO film is that it becomes too absorbing in the near infrared (IR). Silver has good optical characteristics however it reacts with the oxygen in the air and causes the electrodes to deteriorate or oxidize over time. In addition, the thickness of this electrode has to be less than 30nm because values larger than this decrease transmission. From the design of the samples, the first electrode being deposited has to allow a substantial amount of light through the electrode in order for the light to interact with the polymer. ITO and gold were used in the creation of the majority of the samples. Gold does not react with the environment and the optical properties are well known. Again, to manage the losses the film thickness has to be kept to less than 30nm for the same reasons as silver.

Electron Beam (E-Beam) deposition can also be used. One advantage of using E-Beam deposition is that the edge profiles of the shadow mask can have a more defined aspect ratio. Usually the target is small and a few inches away from the sample. It can be treated as a point source. Due to this phenomenon the edge profiles are more crisp and defined. DC or RF sputtering typically has larger targets, greater than 4 inches, which deposits the material more uniformly in all directions. This leads to a more rounded edge thickness profile. This process was not needed due to the design of the bulk electrodes

that were patterned onto the samples. No matter what deposition method is used, one must pay attention to the film thickness. At all times calibration or verification must be done in order to maintain the thickness standards.

The Poling Process

After the sample has been made, the sample must be poled when using a higher glass transition temperature, T_g, polymer such as PMMA. The polling process can vary depending on which method is used. The goal of polling is to align the chromophores in the polymer layer in one direction. This is typically done by applying an electric field across the polymer layer (about 100 volts per micron, V/ μm) and heating the polymer to the T_g temperature. As stated earlier, once the polymer has reached T_g, the material becomes more elastic and this allows the chromophore molecules to align themselves in the presence of the electric field. Corona poling or contact polling are two common ways of aligning the chromophores in the polymer matrix.

Corona Poling

Corona poling is the process where a very high electric field gradient is produced in an atmospherically controlled environment such as nitrogen. The sample is then placed in this electric field gradient and heated to achieve the results. Some issues with this process is knowing exactly what the electric field gradient is in order to know what poling field, V/um, was achieved. This process usually requires very high voltages and arcing is always a concern. Controlling the temperature is also another design parameter that needs to be considered. One advantage to this is that there is no need for making contact of the electrodes to a voltage source.

Contact Poling

Contact poling was used to make our samples. The main difference here is that there is a direct connection of the, slightly less, high voltage power supply to the sample. Knowing the thickness of the polymer layer is needed in order to achieve the proper poling field. These samples were made with a 2 μm thick polymer layer. Knowing this, we applied a voltage of 150 V in order to obtain a 75 V/μm poling field. This is slightly less than ideal, 100 V/μm, however optimizing the performance can be attained once more variables in the process are understood.

CHAPTER V

RESULTS

After all the complications inherent in sample preparation were brought under control, sample measurements were performed. Initially within a standard Teng and Man cross-polarized configuration, the sample was not producing any usable signal. After some investigation the electrodes proved to be causing the degraded signal. ITO was selectively absorbing and scattering the TE polarization. Now this configuration is designed to produce a phase modification on the circularly polarized light that is hitting the analyzer. This was going to be accomplished by inducing a change in the index needed to shift the phase of the polarizations by some amount. This will cause the circularly polarized light to become elliptical in nature. The analyzer that is located before the detector, which is cross-polarized in reference to the input beam, would then pick out this newly acquired intensity due to the phase change from circular to elliptical polarization. The amplitude of the light would then be different then that of the circularly polarized light and thus producing a modulation. Since one of the polarizations is absorbed by more than 90%, the idea either had to be modified and possibly designed with different electrodes or abandoned. Since the losses of the electrodes are too much for phase modulation, we choose to switch to an amplitude modulation scheme and keep the device configuration. There are some additional losses such as scattering associated

with the polymer layer that further compound and magnify the total losses of the system. When the sample is on resonance, these losses are magnified even more. Many devices utilize some sort of lumped element electrode such as ITO and gold. One obvious source of the losses in our devices stems from the second electrode itself which we used as either gold or ITO. After initial deposition of gold the film is optically uniform. Smooth, no cracks, and mirror like even under a microscope. However after poling, the electrode exhibits hazing, cracking, and a lot of surface roughness. One of the reasons for this surface roughness comes from the difference in the coefficient of thermal expansion.

One result of interest is that with this setup, similar to Teng and Man, we can measure the EO coefficients in a similar manner. Also Attenuated Total Reflection (ATR) can be constructed and performed with this experimental setup. ATR can also be used to quantify the devices EO activity.

Next we proceeded to remove the analyzer and look for the amplitude modulation. Given the loading of 8% DR1 to PMMA, a poling field of 50 V/um, and a device construction consisting of asymmetric electrodes of ITO and gold for the second outer reflecting electrode, we obtained a r_{33} value of 0.3 pm/V. This result is low. Currently other EO chromophores may have an activity as high as 100 pm/V. Figure 5.1 shows the device data for the angular scans. The electrodes on this sample are 100 nm thick and the polymer layer is 2um thick. In order to measure an electro-optic coefficient as stated above, the Teng and Man method could be used. Since we are dealing with a prism, there is a slight alteration that needs to be done to the math. Since our samples are made out of prisms, standard samples were made on glass slides in the same configuration as the ones on the prism.
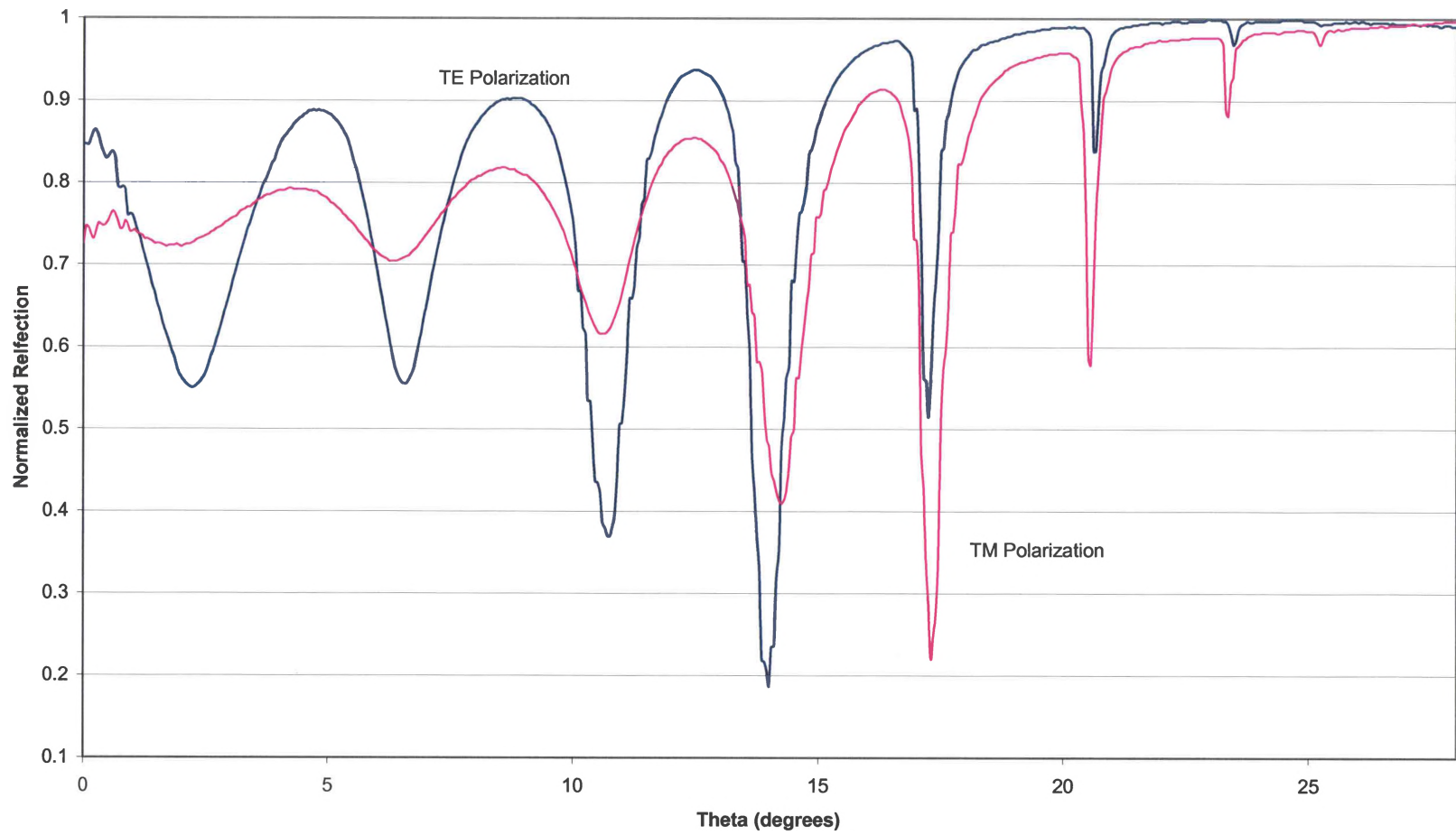
Figure 5.1: Angular scan data

Then the Teng and Man method can be utilized as stated in the literature. The depth of modulation that we were able to obtain is .01%. The experiment was performed with a 50 V applied signal from the function generator. From the theoretical result in Eq. (2.43) we stated a modulation depth of 0.02%, which is good agreement with our experiment. Originally the goal was to have a modulation scheme that operated on less than five volts. This result was obtained at nearly ten times that goal.

The Teng and Man method is used to measure the effective electro-optic activity, or r_{33} value. Similar to the setup described above for phase modulation, we want equal amounts of TE and TM polarization components striking the sample. This is easily done with a polarizer with its pass axis at 45° to the table followed by the compensator. Also the sample is placed at a known angle, usually 45°, to the orientation of the laser being used. Given a standard sample geometry on a glass slide as stated in the literature for measuring the EO activity, the measurement can be performed with the addition of a Soleil-Babinet compensator followed by an analyzer in the reflected beams path before the detector. Now the proper adjustments can be made in order to calculate the electro-optic activity. The intensity needs to be adjusted such that you are operating in the linear region of the response curve for the two orthogonal polarizations. This means that you need to use the compensator in order to adjust the phase of the two polarizations in order to be at the midpoint of the intensity profile.

Figure 5.2 shows a response curve of intensity versus phase to optimize the bias voltage in the Teng and Man setup. As the intensity of the light varies on the detector, the voltage output on the detector will vary. The desired optimal voltage is known as the bias voltage, or V_{bias}, and is found by the given equation:

43

$$V_{bias} = \frac{V_{max} - V_{min}}{2} + V_{min} \qquad (5.1)$$

Once the correct V_{bias} is obtained, all that is needed is the function generators

amplitude, $V_{applied}$, and the amplitude of the signal found from the lock-in amplifier,

ΔV. With these measurements and the following equation, an r_{33} value for the sample

can be obtained.

$$r_{33} = \frac{3\lambda}{4\pi n^2} \frac{\sqrt{n^2 - \sin^2\theta}}{\sin^2\theta} \frac{\Delta V}{V_{applied} \bullet V_{bias}} \qquad (5.2)$$

λ is the wavelength of the laser being used, n is the index of the polymer film, θ is 45°,

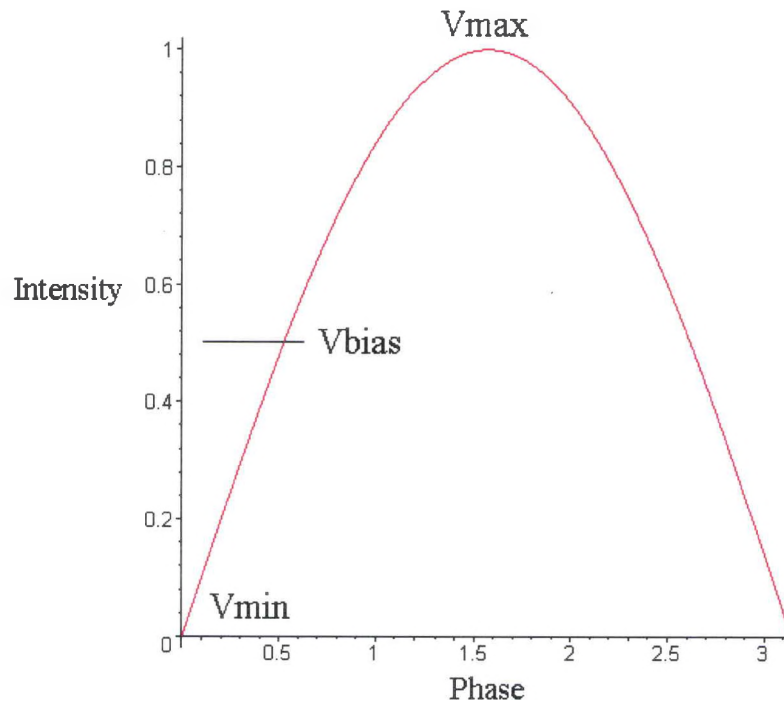and all of the voltages are known.

Figure 5.2: Detector response Curve for the Teng and Man setup.

Another optical phenomenon that we attempted to measure is the Goos-Hänchen shift. It is known that upon reflection that the two polarizations experience a lateral shift known as the Goos-Hänchen shift, which has a different value for each polarization. Our experiment measured the difference between these two displacements. The reason this was looked at is because the Goos-Hänchen shift has the possibility of obtaining large phase changes that could be utilized in order to use this device in a phase modulation scheme as initially thought of. This is achieved by the optical path difference that is measured. As the beam traverses the optical path it acquires a certain phase. If this optical path can be controlled, then the phase that it acquires can be controlled and utilized in such a way to cause destructive interference. It is well known that the orthogonal polarizations interact differently given a single set of boundary conditions. The details of this behavior are explained using the solutions to Maxwell's equations. The shifts we observed in one experiment is seen in figure 5.3. We modified the polarizer in the setup such that it was rotated from 0° to 90° and back. By keeping the sample at the same angular position and recording the intensity profiles as before with an alternating TE and TM beam polarizations, the intensity profiles do not sit on top of each other but rather are displaced by a small angular amount due to the different Goos-Hänchen shifts. This angular data can be used in a $r \bullet \theta$ relationship in order to obtain the linear difference in the shift of the reflected beam between the two polarizations. Figure 5.3 plots a measurement of the Goos-Hänchen shift for TE and TM polarizations. The relative difference in their shift is 0.02°. Now since the time involved with this project did not allow any further maturation into using the Goos-Hänchen shift, we did not pursue its use and it is simply stated as a result.
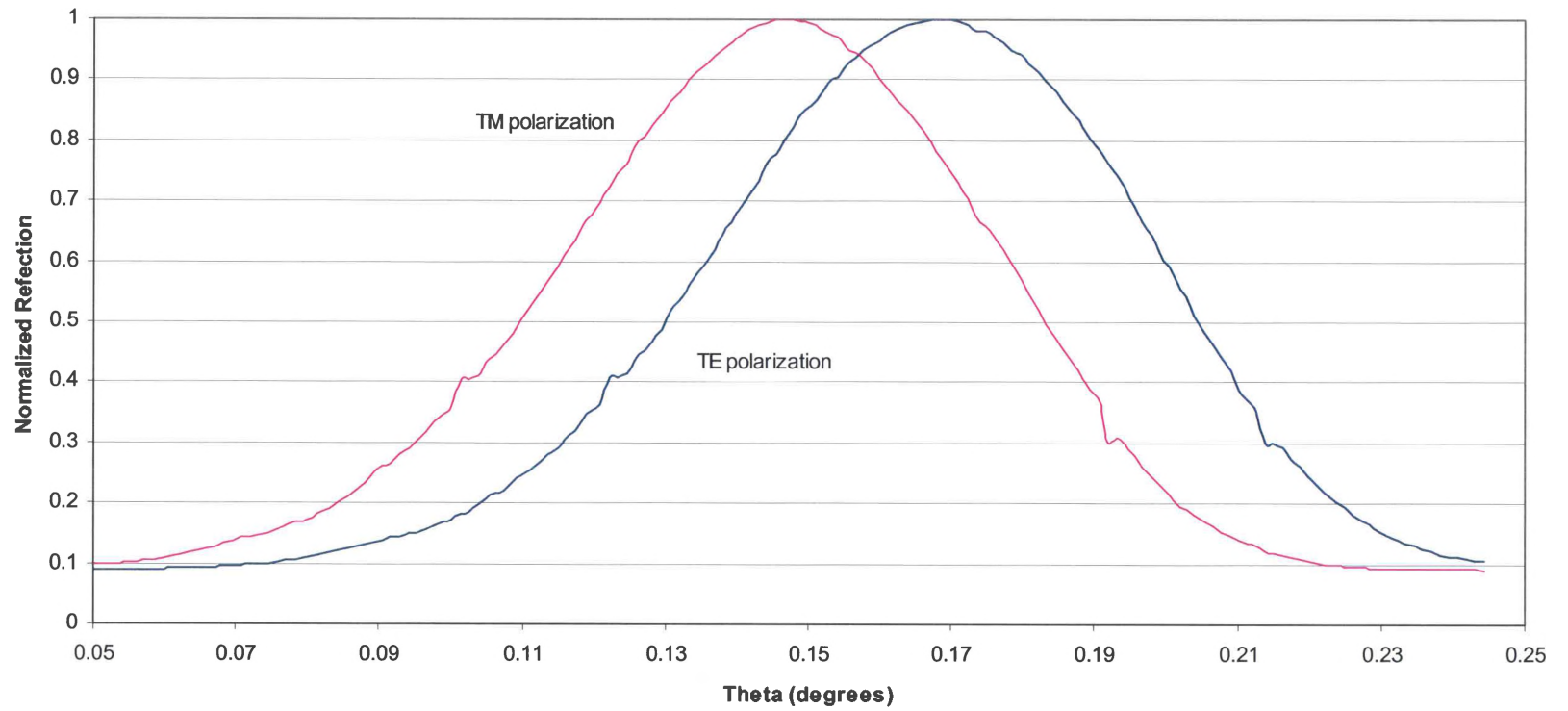
Figure 5.3: Observed relative Goos-Hänchen shift for two polarizations.

The experimental results correlated well with the modeling. Exact agreement is very difficult to obtain due to effects such as scattering and surface quality being difficult to incorporate into theory. Figure 5.4 shows how the modeling compares to the experimental results. The theory is shown in red while the sample measurements are shown in blue.
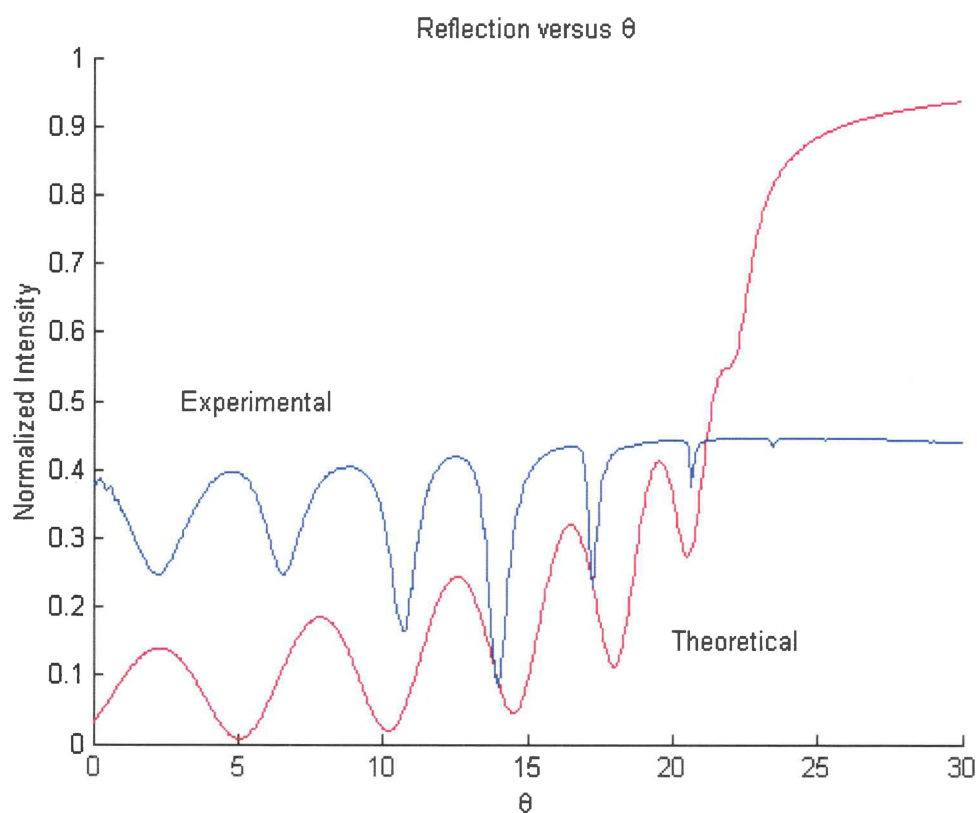
Figure 5.4: Experimental versus theory correlation. Theta is given in reference to the external angle of the beam in air refracting into the prism.

The angular position of the data is relatively close. Total internal reflection can be found and compared easily by adjusting the index of the polymer film. The samples are very sensitive to the optical parameters such as index, loss, and thickness. Minor adjustments, on the order of 10^{-3}, to any of these parameters will produce noticeably different results.

By adjusting the index of the polymer film, the total internal reflection phenomena can be used as a marker to base comparisons between the theory and experiment. Aligning these locations in the data can help determine the samples actual index as it will vary slightly. Adjusting the thickness will alter the number of resonances in the data. The loss terms can vary the depth of the resonances and the overall peak intensity. Scattering of the beam through the sample was not included in the modeling. Scattering is present and is one of the reasons why the experimental intensity does not go to unity at the critical angle. This effect is seen easily by putting a white viewing screen in the beams monitored output. What appears is not a gaussian intensity profile but rather a diffused spot with a random speckle pattern. Surface roughness associated with the films after poling also contributes to these phenomena [14, 15].

CHAPTER VI

CONCLUSIONS

After covering all the experimental results, there is a lot that can be said about this research. The theoretical analysis and the experimental results do show similar trends. The experimental results can be correlated well with the theory. However obtaining exact agreement of the two is much more difficult to achieve. The dichroic behavior shown by the electrodes had significant negative affects on the device. The deposited ITO strongly absorbed the TE polarization thus reducing the phase modulation effectiveness. Altering the oxygen content during the sputtering process can vary the resistivity and optical clarity of the ITO films. This was attempted and the results were the same. It is also well known that DR1 has an absorption line near the operating wavelength of a helium neon laser, 632.8 nm. While this is of concern, I never obtained results that were significant enough to warrant a switch to a longer operating wavelength. There is also some loss associated with the electrodes. The imaginary part of the index of refraction was taken into consideration and incorporated into the modeling as done in the previous chapters. The experimental results did show some added loss that was indicated in the intensity profile that was greater than what the modeling showed. The absorption line of DR1, the dispersion of the polymer film, and the surface quality of the last electrode on the polymer film aided this. Although filtering was done on the polymer film down to 0.2 μm and the films were spin coated in a clean room, there is still room

for particles and contaminates to be introduced into the film. These were seen after processing and all stages throughout the research and at varying levels. Lastly the surface quality of the outer electrode was less than ideal after poling. After the samples were taken out of the sputter chamber for the last electrode, they looked very smooth with little to no visual surface roughness and or haziness. After poling there was an obvious distortion of the electrode layer due to the difference in the coefficient of thermal expansion for the ITO and PMMA. With all of these parameters working against us, I was still able to obtain reproducible results. However the initial idea of a phase modulator was mostly altered into an amplitude modulator due to the strong dichroic absorption of the ITO. The amplitude modulation did yield reproducible results, however with the current material construction of the device, achieving a modulation scheme that is compact with smaller electrical requirements and high speed frequency operation needs more attention paid to the loss mechanisms. The theoretical analysis estimates a very low depth of modulation that was verified in the experiment. The modeling and experimental data agrees to a certain extent and therefore we feel that we have a good idea of what is happening in the structure. Unforeseen loss mechanisms such as surface roughness, scattering, and absorption which are more difficult to incorporate into a modeling algorithm offer good reasons why the two plots have some differences. More research can be done utilizing the Goos-Hänchen shift and possibly exploring different electrode materials that exhibit low loss.

REFERENCES

1. P. Tournois, "Negative group delay times in frustrated Gires-Tounrois and Fabry-Perot Interferometers, " *IEEE Journal of Quantum Electronics*, **33** (4) 519-526 (1997).

2. J. Homola, S. S. Yee, G. Gauglitz, "Surface plasmon resonance sensors: review," *Sensors and Actuators*, **B54** 3-15 (1999).

3. E. Kretschmann, H. Raether, "Radiative decay of non-radiative surface plasmons excited by light," *Zeitschrift für Naturforschung*, **23A** 2135-2136 (1968).

4. A. Otto, "Excitation of surface plasma waves in silver by the method of frustrated total reflection," *Zeitschrift für Naturforschung,* **216** 398-410 (1968).

5. Y Levy, M. Dumont, E. Chastaing, P. Robin. P. A. Chollet, G. Gadret, F Kajzar, "Reflection Method for Electro-optical Coefficient Determination in Statified Thin Film Structures," *Molecular Crystal and Liquid Crystal Science Technology*. Section B **4** (1) (1993).

6. R. Kaiser, Y. levy, J. Fleming, S. Muniz, V. S. Bagnato, "Resonances in a single thin dielectric layer: Enhancement of the Goos-Hänchen shift," *Pure and Applied Optics* **5** (6), 891-898 (1996).

7. K. Resch, J. S. Lundeen, A. M. Steinberg, "Total Reflection cannot occur with a negative time delay," IEEE *Journals of Quantum Electronics*, **37** (6) 794-799 (2001).

8. 7. P. Yeh, "Optical waves in layered media," Wiley Interscience (2005).

9. E. Hecht, "Optics, Fourth edition," Addison Wesley (2002).

10. M. Born, E. Wolf, "Principles of Optics," Cambridge University Press, 4th Edition, (1998).

11. E. D. Palik, "Handbook of optical constants," Academic Press (1998).

12. K. K. Schuegraf, "Handbook of thin-film deposition processes and techniques: principles, methods, equipment, and applications," Noyas Publications (1988).

13. O. J. Sweeting, "The science and technology of polymer films," Interscience Publishers (1968-71).

14. R. L. Nelson, R.W. Boyd, "Enhanced third-order nonlinear optical response of photonic bandgap materials," *Journals of Modern Optics* **46** (7), 1061-1069 (1999).

15. R. L. Nelson, J. W. Haus, B. Birchfield, J. G. Grote, F. K. Hopkins, D. E. Diggs, J. S. Zetts, "Polymeric resonant structures in the reflection geometry for electro-optic modulation and sensing," *SPIE, Organic photonic materials and device*, **4991** 158-165 (2003).

APPENDICES

Appendix A

Matlab modeling code:

```
clear all;

clc;

res=601;

n1=1.778;

n2=1.5+.003i;

n3=1.94+.01i;

lambda=.6328;

k0=2*pi/lambda;

d=2.65;

phi=k0*d;

theta=linspace(pi/4,1.070457973,res);

for x=1:res;

  Input=[1 n1*cos(theta(x)) 0 0];

  theta1=asin(n1*sin(theta(x))/n2);

  theta2=asin(n2/n1*sin(theta1));
```

```
bcte=[-1 n1*cos(theta(x)) 0 0;1 n2*cos(theta1) exp(i*phi*n2*cos(theta1)) -

n2*exp(i*phi*n2*cos(theta1))*cos(theta1);1 -n2*cos(theta1) exp(-i*phi*n2*cos(theta1))

n2*exp(-i*phi*n2*cos(theta1))*cos(theta1);0  0 -exp(i*phi*n3*cos(theta2))

n3*exp(i*phi*n3*cos(theta2))*cos(theta2)];

  Outputte=Input*inv(bcte);

  Intensity(:,:,x)=Outputte.*conj(Outputte);

  R0(x)=Intensity(1,1,x);

  T0(x)=Intensity(1,2,x)*n2/n1;

  R1(x)=Intensity(1,3,x);

  T1(x)=Intensity(1,4,x)*n3/n2;

end

plot(theta8*180/pi,R0,'r')

title('Reflection versus Theta')

xlabel('\theta')

ylabel('Normalized Intensity')
```

VITA

February 1, 1979	Born – Oberlin, Ohio
1999	Associate of Science, Lorain County Community College, Lorain, Ohio
2002	B.S. Physics, University of Toledo, Toledo, Ohio
2000-2002	Research assistant, First Solar LLC, Perrysburg, Ohio
2006	M.S. Electro Optics, University of Dayton, Dayton, Ohio
2002-2006	Graduate Assistant, University of Dayton, Dayton Ohio. Graduate Assistant, Air Force Research Laboratory, WPAFB, Ohio

PUBLICATIONS/CONFERENCE APPEARANCES

B. Birchfield, R. Nelson, J. Haus, P. Yaney, Electro-optic effective medium composite materials, 2005 Joint Spring Meeting Ohio Section of APS, April 8-9, 2005.

B. Birchfield, R. Nelson, J. Haus, Novel nonlinear electro-optic composite materials (6123-04), Photonics West 2006 January 21-26 (2006).

R. Nelson, J. Haus, B. Birchfield, Polymeric nonlinear optical devices (6123-06), Photonics West 2006 January 21-26 (2006).

FIELDS OF STUDY

Major field; Electro-optic thin film devices

Nonlinear electro-optic thin film modulation, Professor Joseph Haus and colleague Robert Nelson

Polymer thin film devices, Professor Joseph Haus and colleague Robert Nelson.